

# A TWO-DIMENSIONAL PLASMA ACTUATOR ANALYSIS CODE

---

**Steven Ellison**

**Air Force Research Laboratory  
Munitions Directorate  
AFRL/MNAC  
101 W. Eglin Blvd.  
Eglin AFB FL 32542-6810**



**JANUARY 2006**

**INTERIM REPORT FOR PERIOD NOVEMBER 2004 - NOVEMBER 2005**

**DISTRIBUTION A - Approved for public release; distribution unlimited.**

**AIR FORCE RESEARCH LABORATORY, MUNITIONS DIRECTORATE**

**Air Force Materiel Command ■ United States Air Force ■ Eglin Air Force Base**



## NOTICE

When Government drawings, specifications, or other data are used for any purpose other than in connection with a definitely Government-related procurement, the United States Government incurs no responsibility or any obligation whatsoever. The fact that the Government may have formulated or in any way supplied the said drawings, specifications, or other data, is not to be regarded by implication, or otherwise in any manner construed, as licensing the holder, or any other person or corporation; or as conveying any rights or permission to manufacture, use, or sell any patented invention that may in any way be related thereto.

This technical report is releasable to the National Technical Information Services (NTIS). At NTIS it will be available to the general public, including foreign nations.

This technical report has been reviewed and is approved for publication.

FOR THE COMMANDER

//Signature//

Frederick A. Davis  
Technical Director,  
Assessment and Demonstrations Division

//Signature//

Steven Ellison  
Aerospace Engineer,  
Computational Mechanics Branch

Anyone having need of a copy of this report should first contact the Defense Technical Information Center (DTIC) at the address shown below. If you are a registered DTIC User and qualify as a recipient of this document, DTIC can provide you with a copy. If you are a registered DTIC User and do not qualify as a recipient, DTIC can submit a request for release, on your behalf, to the controlling DoD agency for their review and determination. Please do not request copies from the Air Force Research Laboratory, Munitions Directorate. Requests for additional copies should be directed to:

Defense Technical Information Center (DTIC)  
8725 John J. Kingman Road, Ste 0944  
Ft Belvoir, VA 22060-6218

This report is published in the interest of the scientific and technical information exchange. Publication of this report does not constitute approval or disapproval of the ideas or findings. Do not return copies of this report unless contractual obligations or notice on a specific document requires its return. If you no longer have a need to retain this document, please refer to the Destruction Notice on the cover page for instruction.



# REPORT DOCUMENTATION PAGE

*Form Approved*  
*OMB No. 0704-0188*

Public reporting burden for this collection of information is estimated to average 1 hour per response, including the time for reviewing instructions, searching existing data sources, gathering and maintaining the data needed, and completing and reviewing this collection of information. Send comments regarding this burden estimate or any other aspect of this collection of information, including suggestions for reducing this burden to Department of Defense, Washington Headquarters Services, Directorate for Information Operations and Reports (0704-0188), 1215 Jefferson Davis Highway, Suite 1204, Arlington, VA 22202-4302. Respondents should be aware that notwithstanding any other provision of law, no person shall be subject to any penalty for failing to comply with a collection of information if it does not display a currently valid OMB control number. **PLEASE DO NOT RETURN YOUR FORM TO THE ABOVE ADDRESS.**

<b>1. REPORT DATE</b> ( <i>DD-MM-YYYY</i> ) 11-01--2006		<b>2. REPORT TYPE</b> INTERIM		<b>3. DATES COVERED</b> ( <i>From - To</i> ) Nov 2004 – Nov 2005	
<b>4. TITLE AND SUBTITLE</b> A Two-Dimensional Plasma Actuator Analysis Code				<b>5a. CONTRACT NUMBER</b>	
				<b>5b. GRANT NUMBER</b>	
				<b>5c. PROGRAM ELEMENT NUMBER</b> 61102F	
<b>6. AUTHOR(S)</b> Ellison, Steven				<b>5d. PROJECT NUMBER</b> 2307	
				<b>5e. TASK NUMBER</b> BN	
				<b>5f. WORK UNIT NUMBER</b> 05	
<b>7. PERFORMING ORGANIZATION NAME(S) AND ADDRESS(ES)</b>  Air Force Research Laboratory, Munitions Directorate AFRL/MNAC 101 W. Eglin Blvd. Eglin AFB, FL 32542-6810				<b>8. PERFORMING ORGANIZATION REPORT NUMBER</b>  AFRL-MN-EG-TR-2006-7006	
<b>9. SPONSORING / MONITORING AGENCY NAME(S) AND ADDRESS(ES)</b> Air Force Research Laboratory, Munitions Directorate AFRL/MNAC 101 W. Eglin Blvd. Eglin AFB, FL 32542-6810				<b>10. SPONSOR/MONITOR'S ACRONYM(S)</b> AFRL-MN-EG	
				<b>11. SPONSOR/MONITOR'S REPORT NUMBER(S)</b> AFRL-MN-EG-TR-2006-7006	
<b>12. DISTRIBUTION / AVAILABILITY STATEMENT</b>  Approved for public release; distribution unlimited					
<b>13. SUPPLEMENTARY NOTES</b>					
<b>14. ABSTRACT</b> A two-dimensional plasma actuator analysis code has been developed. A time-accurate Navier-Stokes CFD code was coupled with a time-dependent, phenomenological model of an alternating current, single dielectric barrier discharge plasma actuator. The accuracy of the flow solver was demonstrated using a standard CFD validation case. The plasma actuator model's ability to affect fluid motion was tested by inducing motion in quiescent air over a flat plate using only the plasma actuator model. The resulting fluid motion was similar to the induced motion observed in plasma actuator experiments.					
<b>15. SUBJECT TERMS</b> Plasma, plasma actuator, single dielectric barrier discharge, computational fluid dynamics					
<b>16. SECURITY CLASSIFICATION OF:</b>			<b>17. LIMITATION OF ABSTRACT</b>	<b>18. NUMBER OF PAGES</b>	<b>19a. NAME OF RESPONSIBLE PERSON</b>
<b>a. REPORT</b>	<b>b. ABSTRACT</b>	<b>c. THIS PAGE</b>			Steven Ellison
UNCLASSIFIED	UNCLASSIFIED	UNCLASSIFIED	Unlimited	25	<b>19b. TELEPHONE NUMBER</b> ( <i>include area code</i> ) (850) 883-2687



## **ABSTRACT**

A two-dimensional plasma actuator analysis code has been developed. A time-accurate Navier-Stokes CFD code was coupled with a time-dependent, phenomenological model of an alternating current, single dielectric barrier discharge plasma actuator. The accuracy of the flow solver was demonstrated using a standard CFD validation case. The plasma actuator model's ability to affect fluid motion was tested by inducing motion in quiescent air over a flat plate using only the plasma actuator model. The resulting fluid motion was similar to the induced motion observed in plasma actuator experiments.



## TABLE OF CONTENTS

INTRODUCTION .....	1
TECHNICAL APPROACH.....	2
Equations of Fluid Motion .....	3
Finite Volume Formulation.....	4
Central Differencing.....	5
Artificial Dissipation.....	6
Explicit Time Integration .....	7
Accelerating Convergence .....	8
Dual Time-Stepping.....	9
Turbulence Model.....	9
Plasma Actuator Model.....	10
RESULTS .....	14
RAE 2822 Airfoil.....	14
Flat Plate with Plasma Actuator .....	16
CONCLUSION AND RECOMMENDATIONS.....	16
REFERENCES .....	20
ACKNOWLEDGEMENTS .....	21



## INTRODUCTION

Aerodynamic flow control by means of plasma actuators is an active area of research in the Air Force and in academia. Experiments have shown that these devices can be used to induce flow movement in a stationary air mass, and to reattach separated flow on airfoils at high angles of attack. Plasma actuators offer potential advantages in weight reduction, cost, and manufacturability over traditional flow control devices such as slats and flaps<sup>1</sup>.

Plasma actuators consist of two electrodes separated by a dielectric material. The electrodes are offset, with one electrode exposed to the air and the other embedded in the dielectric material as shown in Figure 1. When a high voltage alternating current is applied to the electrodes, the air above the insulated electrode ionizes, beginning at the edge of the exposed electrode and spreading across the insulated electrode. The extent to which the plasma field covers the insulated electrode increases and decreases with the rising and falling voltage. The ionized region produces a “body force”, which induces motion in the surrounding air<sup>2</sup>.

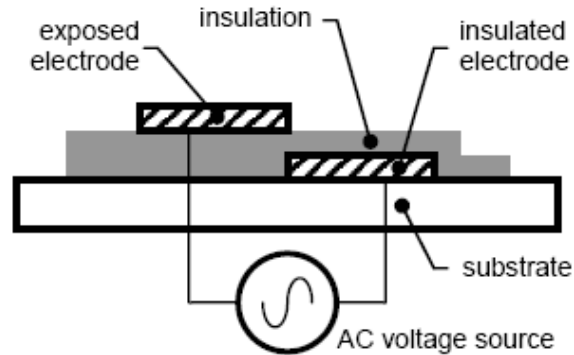


**Figure 1: Plasma Actuator Schematic<sup>3</sup>**

In FY 2004-2005, AFOSR sponsored AFRL/MNAC to perform research into the effectiveness of plasma actuators as aerodynamic control devices. The ultimate objective of this research was to model the effects of plasma actuators on aerodynamic flow fields by incorporating a first-principles plasma generation model into a Navier-Stokes flow solver. Both the plasma code and the flow solver code were under development in FY 2004-2005. While the flow solver had been successfully demonstrated on several standard validation cases, development of the plasma code had not progressed to the point that it could be incorporated into the flow solver. Because of this, AFRL/MNAC initiated a collaborative agreement with AFOSR-sponsored researchers at the University of Notre Dame to incorporate a plasma actuator model developed there into the AFRL/MNAC flow solver.

The Notre Dame model may best be described as *phenomenological*. While this model does not simulate the creation and motion of ions in the plasma field, it does a credible job generating force fields that induce the type of motion observed in plasma actuator experiments. Instead of simulating the plasma field, this model represents the region over the insulated electrode as a set of parallel electronic circuits, such as the one shown in Figure 2, distributed along the insulated electrode. The circuit capacitances and resistances are derived

from both experimentally determined and inferred electrical properties of air. The individual circuits are activated when the voltage difference between the exposed and insulated electrodes exceeds a critical threshold. In this way the advance and retreat of the plasma field is simulated as the applied voltage oscillates.

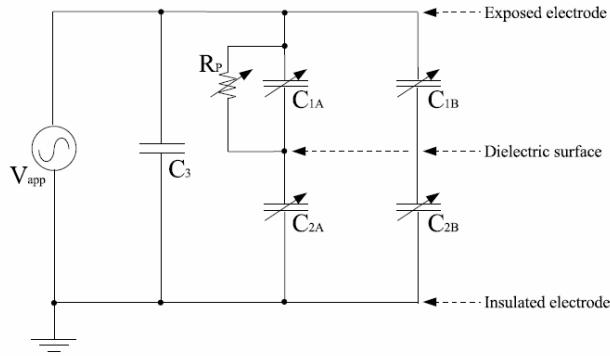


**Figure 2: Plasma Actuator Circuit Model<sup>2</sup>**

The voltage distribution resulting from the solution of the time-varying circuit equations is used on the boundary of a two-dimensional Poisson equation solver that computes the electric potential in the vicinity of the plasma actuator. A body force field calculated from this electric potential is used in the Navier-Stokes flow solver to induce motion in the flow.

The remainder of this report will describe the solution algorithms employed in the two-dimensional Navier-Stokes flow solver with the integrated plasma actuator model. Several example solutions will be presented to demonstrate the flow solver’s capability.

### TECHNICAL APPROACH

The flow solver developed in this effort solves the Navier-Stokes equations of fluid motion using simple numerical algorithms. Although solution times could be reduced by using more complicated solution techniques, simple algorithms were chosen in order to reduce the effort required to understand the code well enough to perform modifications.

Since the purpose of this research effort was to study the effects of plasma actuators on air flows, extraordinarily high solution fidelity was not a requirement. The flow solver was only required to produce solutions of sufficient fidelity that the effects of the plasma actuator on the flowfield could be studied.

In this finite-volume flow solver, the spatially varying terms are discretized using central differencing<sup>4</sup> stabilized with flux-limiting numerical dissipation<sup>5</sup>. Turbulent terms are computed using the so-called “detached eddy simulation” version of the Spalart-Allmaras turbulence model<sup>6</sup>. Temporal integration is performed using the dual-time stepping algorithm<sup>7</sup>. The plasma actuator is simulated using the Notre Dame model<sup>2,8</sup>.

### Equations of Fluid Motion

The two-dimensional Navier-Stokes equations of fluid motion in conservation law form, accounting for body forces, are<sup>9</sup>

$$\frac{\partial Q}{\partial t} + \frac{\partial E}{\partial x} + \frac{\partial F}{\partial y} = S \quad (1)$$

or

$$\frac{\partial Q}{\partial t} + \frac{\partial(E_i - E_v)}{\partial x} + \frac{\partial(F_i - F_v)}{\partial y} = S \quad (2)$$

where  $Q$ ,  $E$ ,  $F$ ,  $G$ , and  $S$  are vectors:

$$\begin{aligned} Q &= \begin{Bmatrix} \rho \\ \rho u \\ \rho v \\ \rho E \end{Bmatrix} & S &= \begin{Bmatrix} 0 \\ f_x \\ f_y \\ f_x u + f_y v \end{Bmatrix} \\ E_i &= \begin{Bmatrix} \rho u \\ \rho u^2 + p \\ \rho uv \\ \rho Hu \end{Bmatrix} & E_v &= \begin{Bmatrix} 0 \\ \tau_{xx} \\ \tau_{xy} \\ u\tau_{xx} + v\tau_{xy} + q_x \end{Bmatrix} \\ F_i &= \begin{Bmatrix} \rho v \\ \rho uv \\ \rho v^2 + p \\ \rho Hv \end{Bmatrix} & F_v &= \begin{Bmatrix} 0 \\ \tau_{xy} \\ \tau_{yy} \\ u\tau_{xy} + v\tau_{yy} + q_y \end{Bmatrix} \end{aligned} \quad (3)$$

The shear stresses ( $\tau_{**}$ ) and heat fluxes ( $q_*$ ) in Eq (3) are given by:

$$\tau_{xx} = \frac{2}{3}\mu \left( 2\frac{\partial u}{\partial x} - \frac{\partial v}{\partial y} \right) \quad \tau_{yy} = \frac{2}{3}\mu \left( 2\frac{\partial v}{\partial y} - \frac{\partial u}{\partial x} \right) \quad \tau_{xy} = \mu \left( \frac{\partial u}{\partial y} + \frac{\partial v}{\partial x} \right) \quad q_x = k \frac{\partial T}{\partial x} \quad q_y = k \frac{\partial T}{\partial y} \quad (4)$$

The gas properties appearing in Eqs (3)-(4) are:

$\rho$	Density
$u, v$	Cartesian velocity components
$E$	Total energy
$f_x, f_y$	Cartesian body force components (per unit volume)
$p$	Pressure
$H$	Total enthalpy ( $E + p/\rho$ )
$T$	Temperature
$\mu$	Coefficient of viscosity
$k$	Coefficient of thermal conductivity

Two equations of state can be used to relate the fluid properties:

$$p = (\gamma - 1) \left[ \rho E - \frac{1}{2} \rho (u^2 + v^2) \right] \text{ or } p = \rho RT \quad (5)$$

### Finite Volume Formulation

The Navier-Stokes equations are solved using a cell-centered finite volume (FV) formulation. In the FV scheme, the domain of interest is subdivided into small control volumes, or cells. A portion of a two-dimensional computational grid is shown in Figure 3. The details of this diagram will be explained in the following discussion.

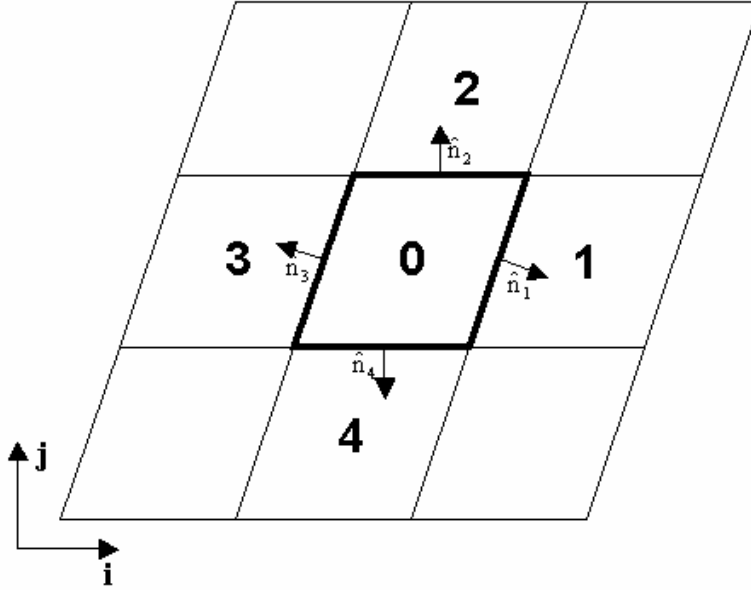


**Figure 3: A Portion of a Two-Dimensional Computational Grid**

The fluid properties are assumed to be constant throughout a particular grid cell at any time during the solution process. Temporal changes in the cell fluid properties are determined by tracking the flux of the fluid properties across the cell boundaries. Eq (1) can be expressed as

$$\frac{\partial Q}{\partial t} + \vec{\nabla} \cdot (\mathbf{E}\hat{i} + \mathbf{F}\hat{j}) = S \quad (6)$$

Treating the fluid properties within a cell as constant and integrating Eq (6) over the cell volume  $V$  yields

$$V \frac{\Delta Q}{\Delta t} + \iiint_{\text{Vol}} \vec{\nabla} \cdot (\mathbf{E}\hat{i} + \mathbf{F}\hat{j}) dV = VS \quad (7)$$

where  $\Delta(\bullet)$  indicates a discrete change in the indicated quantity. Gauss' theorem can be used to convert the volume integral of Eq (7) into a surface integral:

$$V \frac{\Delta Q}{\Delta t} + \sum_{N=1}^{Nf} (\mathbf{E}\hat{i} + \mathbf{F}\hat{j}) \cdot \hat{n}_N A_N = VS \quad (8)$$

In Eq (8) the summation is over the bounding faces of the cell, which number  $N_f$ .  $A_N$  is the area of bounding face N, and  $\hat{n}_N = n_x \hat{i} + n_y \hat{j}$  is an outward directed unit vector normal to face N (see Figure 1).

The inviscid and viscous terms can be treated separately:

$$V \frac{\Delta Q}{\Delta t} + R_i(Q) - R_v(Q) - VS = 0 \quad (9)$$

where the inviscid and viscous residuals are

$$R_i(Q) = \sum_{N=1}^{N_f} (E_i \hat{i} + F_i \hat{j})_N \cdot \hat{n}_N A_N \quad (10)$$

$$R_v(Q) = \sum_{N=1}^{N_f} (E_v \hat{i} + F_v \hat{j})_N \cdot \hat{n}_N A_N \quad (11)$$

### Central Differencing

In the central difference scheme, Eq (10) can be written

$$R_i(Q) = \sum_{N=1}^{N_f} F(Q)_N A_N \quad (12)$$

where

$$F(Q)_N = (\vec{V}_N \cdot \hat{n}_N) Q_N + p_N \begin{Bmatrix} 0 \\ n_x \\ n_y \\ \vec{V}_N \cdot \hat{n}_N \end{Bmatrix} \quad (13)$$

In Eq (13), subscripted flow properties  $(\bullet)_N$  represent the average value of the indicated flow property at cell face N. For example,

$$\vec{V}_N = \frac{1}{2} (\vec{V}_0 + \vec{V}_n) \quad (14)$$

where  $\vec{V}_0$  is the velocity in the cell under consideration and  $\vec{V}_n$  is the velocity in the cell adjacent to cell 0 at face N (see Figure 1).

The viscous fluxes involve partial derivatives of the Cartesian velocity components and the temperature. The partial derivatives for a fluid property in cell 0 can be calculated from<sup>10</sup>

$$\begin{aligned} \left( \frac{\partial(\bullet)}{\partial x} \right)_0 &= \frac{1}{V_0} \sum_{N=1}^{N_f} (\bullet) (n_x A)_N \\ \left( \frac{\partial(\bullet)}{\partial y} \right)_0 &= \frac{1}{V_0} \sum_{N=1}^{N_f} (\bullet) (n_y A)_N \end{aligned} \quad (15)$$

Here,  $(\bullet)$  represents the property (e.g. T) to be differentiated.

The coefficient of viscosity is calculated from Sutherland's law

$$\mu = \frac{C_1 T^{3/2}}{T + C_2} \quad (16)$$

where

$$C_1 = 1.458 \times 10^{-6} \frac{\text{kg}}{\text{m} \cdot \text{s} \sqrt{\text{K}}}, C_2 = 110.4 \text{ K} \quad (17)$$

The coefficient of thermal conductivity is calculated from

$$k = \frac{\gamma R \mu}{(\gamma - 1) \text{Pr}} \quad (18)$$

where  $\gamma$  is the ratio of specific heats (1.4 for air),  $R$  is the gas constant ( $287 \text{ m}^2/\text{s}^2 \text{ }^\circ\text{K}$  for air), and  $\text{Pr}$  is the laminar Prandtl number (0.72 for air).

The velocity and temperature gradient terms are calculated for each cell using Eqs (15). Then the viscous residual term can be calculated using Eq (11) where, for example

$$(\mathbf{E}_v)_N = \left\{ \begin{array}{c} 0 \\ (\tau_{xx})_N \\ (\tau_{xy})_N \\ u_N (\tau_{xx})_N + v_N (\tau_{xy})_N + (q_x)_N \end{array} \right\} \quad (19)$$

### Artificial Dissipation

Flow solutions calculated using central difference spatial discretization schemes sometimes exhibit a numerical phenomenon known as odd-even decoupling, in which alternating grid points converge to different solutions. In order to stabilize the calculations when solving the Euler or Navier-Stokes equations using a central difference scheme, it is often necessary to add a dissipative term to the FV integral. The numerical dissipation scheme of Yoon and Kwak<sup>5</sup> is used here. This scheme provides stabilizing background dissipation to the central difference discretization, and employs flux limiters to smooth out numerical dispersion around sharp gradients such as shocks.

At each cell interface a dissipative term is added to the flux. At a cell interface in the  $i$ -direction of a structured grid, for example, the dissipative term is

$$d_{i+1/2} = -\alpha_{i+1/2} \left[ \phi(\sigma_{i+1}) \mathbf{e}_{i+3/2} - 2\mathbf{e}_{i+1/2} + \psi(\sigma_i) \mathbf{e}_{i-1/2} \right] \quad (20)$$

In Eq (20), the  $(\bullet)_{i+1/2}$  terms are evaluated at the cell faces and the  $(\bullet)_i$  terms are evaluated at the cell centers. The coefficient is:

$$\alpha_{i+1/2} = \left( \kappa_0 + \kappa_1 v_{i+1/2} \right) \left( |\vec{v} \cdot \vec{n}| + a \right)_{i+1/2} A_{i+1/2} \quad (21)$$

where  $\kappa_0$  provides a threshold dissipation and  $\kappa_1$  ensures adequate dissipation in the vicinity of a shock.  $A_{i+1/2}$  is the cell face area and  $v_{i+1/2}$  is a “pressure switch” that becomes large in the vicinity of a shock:

$$v_{i+1/2} = \max(v_{i-1}, v_i, v_{i+1}, v_{i+2}) \quad (22)$$

$$v_i = \frac{|p_{i+1} - 2p_i + p_{i-1}|}{(p_{i+1} + 2p_i + p_{i-1})} \quad (23)$$

$\phi$  and  $\psi$  are flux-limiting functions:

$$\phi(\sigma) = \begin{cases} 0 & \text{if } \sigma < 0 \\ \sigma & \text{if } 0 \leq \sigma \leq 1 \\ 1 & \text{if } 1 < \sigma \end{cases} \quad (24)$$

$$\psi(\sigma) = \phi\left(\frac{1}{\sigma}\right) \quad (25)$$

where

$$\sigma_i = \frac{e_{i-1/2}}{e_{i+1/2}} \quad (26)$$

and, for example, when computing dissipation for the continuity equation:

$$e_{i+1/2} = \rho_{i+1} - \rho_i \quad (27)$$

### Explicit Time Integration

Eq (9) can be rewritten to indicate numerical integration over a discrete time interval:

$$Q^{n+1} = Q^n - \frac{\Delta t}{V} R(Q)^n \quad (28)$$

where  $R(Q) = R_i(Q) - R_v(Q) - VS$  and the superscripts  $(\bullet)^n$  and  $(\bullet)^{n+1}$  indicate flowfield properties evaluated at the current solution time  $t$  and at the next solution time  $t+\Delta t$ , respectively.

Eq (28) is the single-step Euler explicit time integration from time level  $n$  to time level  $n+1$  and has first order temporal accuracy. Multistage explicit integration schemes have greater temporal accuracy than this single stage scheme. For example, an  $M$ -stage Runge-Kutta scheme has a formal accuracy of  $M$  for a linear equation<sup>11</sup>. In the  $M$ -stage Runge-Kutta scheme, the solution is advanced over the time interval  $\Delta t$  by

$$\begin{aligned} Q^{(0)} &= Q^n \\ Q^{(m)} &= Q^{(0)} - \lambda^{(m)} \frac{\Delta t}{V} R(Q^{(m-1)}), \quad m = 1, 2, \dots, M \\ Q^{n+1} &= Q^{(M)} \end{aligned} \quad (29)$$

Here, the parenthesized superscripts denote the stages of the Runge-Kutta scheme. The weighting factors  $\lambda^{(m)}$  are calculated from

$$\lambda^{(m)} = \frac{1}{M+1-m}, \quad m = 1, 2, \dots, M \quad (30)$$

The allowable time step for stable calculations is a function of wave propagation speed through the grid cells. For time-accurate solutions, the time step  $\Delta t$  is the global minimum of<sup>11</sup>

$$\Delta t \leq \frac{V}{(F_x + F_y)} \quad (31)$$

with

$$\begin{aligned} F_x &= (|u| + C)A_x \\ F_y &= (|v| + C)A_y \end{aligned} \quad (32)$$

where  $V$  is a cell volume,  $C$  is the speed of sound in the cell,  $A_x$  and  $A_y$  are the projected areas of the cell in the  $x$ - and  $y$ -directions. Multistage Runge-Kutta integration allows the time restriction to be relaxed, so the time step calculated using Eq (31) can be multiplied by a factor  $CFL \geq 1$ .

### Accelerating Convergence

Convergence to a steady state solution can be accelerated using local time-stepping and implicit residual smoothing during the Runge-Kutta integration<sup>11</sup>.

Local time-stepping dispenses with global time accuracy by advancing the solution in each cell using the time step calculated for that cell using Eq (31). This drives the global solution error rapidly to zero since the solution errors are propagated through each cell, and hence through and out of the solution domain, at the maximum possible rate.

Implicit residual smoothing gives the explicit time integration scheme an implicit character, allowing solution advancement at time steps greater than indicated by the stability limit of the explicit scheme. A Laplacian smoothing operator is applied:

$$\bar{R}_0 = R_0 + \varepsilon \nabla^2 \bar{R}_N \quad (33)$$

where

$$\nabla^2 \bar{R}_N = \sum_{N=1}^{Nf} (\bar{R}_n - \bar{R}_0) \quad (34)$$

Eq (33) is solved using Jacobi iteration:

$$\begin{aligned} \bar{R}_0^{(0)} &= R_0^n \\ \bar{R}_0^{(m)} &= \frac{\left( R_0^n + \varepsilon \sum_{N=1}^{Nf} \bar{R}_n^{(m-1)} \right)}{1 + \varepsilon \sum_{N=1}^{Nf} 1}, \quad m = 1, 2, \dots, m_{MAX} \\ \bar{R}_0^n &= \bar{R}_0^{(m_{MAX})} \end{aligned} \quad (35)$$

Effective values of the weighting factor  $\varepsilon$  range from 0.5 to 0.8. In Reference 11, the authors reported a doubling of the allowable time step for Euler solutions on unstructured grids by using two Jacobi iterations per Runge-Kutta stage with  $\varepsilon = 0.5$ .

### Dual Time-Stepping

Dual time-stepping (DTS) is an implicit time integration scheme<sup>7</sup>. In DTS, the spatial terms of Eq (6) are discretized at time  $n+1$ , rather than at time  $n$ , and the temporal term is discretized with a three-point backward difference, resulting in the following variation of Eq (9):

$$\mathbf{V} \left( \frac{3\mathbf{Q}^{n+1} - 4\mathbf{Q}^n + \mathbf{Q}^{n-1}}{2\Delta t} \right) = -\mathbf{R}(\mathbf{Q}^{n+1}) \quad (36)$$

This equation is solved by introducing  $\mathbf{Q}^*$ , an approximation to  $\mathbf{Q}^{n+1}$ , and a pseudo-time variable  $t^*$ . The following equation results:

$$\mathbf{V} \frac{\partial \mathbf{Q}^*}{\partial t^*} = -\mathbf{R}(\mathbf{Q}^*) - \mathbf{V} \left( \frac{3\mathbf{Q}^* - 4\mathbf{Q}^n + \mathbf{Q}^{n-1}}{2\Delta t} \right) = -\mathbf{R}^*(\mathbf{Q}^*) \quad (37)$$

Eq (37) can be solved using the explicit Runge-Kutta scheme of Eq (29) with local time-stepping in pseudo-time ( $t^*$ ) and implicit residual smoothing. Time accuracy is ensured by the inclusion of the time derivative term in  $\mathbf{R}^*(\mathbf{Q}^*)$ . Eq (37) is solved iteratively until it converges on a solution for  $\mathbf{Q}^*$ :

1. Set  $k = 0$
2. Set  $\mathbf{Q}^k = \mathbf{Q}^n$
3. Repeat until  $\mathbf{Q}^{k+1} \approx \mathbf{Q}^k$ :
  - a. Solve Eq (37) for  $\mathbf{Q}^{k+1}$  using Eq (29) with local time-stepping and implicit residual smoothing,  $\mathbf{Q}^{(0)} = \mathbf{Q}^k$ , and  $\mathbf{Q}^{k+1} = \mathbf{Q}^{(M)}$
  - b. Set  $k = k + 1$
4. Set  $\mathbf{Q}^{n+1} = \mathbf{Q}^k$

### Turbulence Model

Inclusion of a turbulence model was not originally planned by the MNAC researchers because turbulence was not expected to play a significant role in the flows to be investigated. However, as the code was being evaluated against standard CFD code validation cases, it became apparent that unsteady, separated flowfields were developing in laminar solutions of test cases that were known not to exhibit such behavior. It was decided to incorporate a turbulence model into the flow solver to ensure that the code would produce separated flows only in those cases where it could reasonably be expected to occur.

Turbulent terms are computed using a variation of the Spalart-Allmaras one-equation turbulence model. The Spalart-Allmaras equation, written without transition terms, is<sup>7</sup>:

$$\frac{\partial \tilde{\nu}}{\partial t} + \nabla(\tilde{\nu}\vec{v}) = C_{b1}\tilde{S}\tilde{\nu} + \frac{1}{\sigma} \{ \nabla[(v_L + \tilde{\nu})\nabla\tilde{\nu}] + C_{b2}(\nabla\tilde{\nu})(\nabla\tilde{\nu}) \} - C_{w1}f_w \left( \frac{\tilde{\nu}}{d} \right)^2 \quad (38)$$

Eq (38) is solved for  $\tilde{\nu}$ , from which the turbulent viscosity coefficient can be calculated. The various terms appearing here are defined in References 6 and 7. The variation from the standard Spalart-Allmaras model lies in the  $d$  term which appears explicitly in Eq (38) as well as implicitly in the definitions of several of the other terms in the equation. In the original scheme,  $d$  is the distance from a cell center point to the nearest solid wall boundary point. Here,  $d$  is the smaller of this distance and the local grid spacing. In the near vicinity of a solid wall, Eq (38) behaves as a turbulence model, but away from the wall, it assumes the nature of the subgrid scale closure models used in large eddy simulation codes.

The solution of Eq (38) will not be discussed in great detail here. The spatial discretization is a first order upwind scheme<sup>7</sup>, and the temporal solver is the multistage Runge-Kutta scheme of Eq (29) with local time-stepping. Because Eq (38) depends on the current flow field, it is not solved simultaneously with the Navier-Stokes equations. Rather, Eq (38) is advanced one local time step for each *stage* of the flowfield Runge-Kutta integration. Using this approach, Eq (38) can be driven to a steady-state solution in the limit of a steady-state flowfield solution.

The turbulent viscosity coefficient  $\mu_t$  is calculated from  $\tilde{\nu}$ , and is added to the laminar viscosity coefficient calculated using Eq (16), leading to the following redefinition of  $\mu$ :

$$\mu = \mu_l + \mu_t \quad (39)$$

The coefficient of thermal conductivity for turbulent flow is calculated by

$$k = \frac{\gamma R}{(\gamma - 1)} \left( \frac{\mu_l}{Pr} + \frac{\mu_t}{Pr_t} \right) \quad (40)$$

$Pr_t$  is the turbulent Prandtl number (0.9 for air).

### Plasma Actuator Model

The plasma actuator model provided by the University of Notre Dame uses a distribution of  $N$  parallel electronic circuits, as shown in Figure 3, to simulate the response of the region above the insulated electrode to an applied voltage<sup>8</sup>. Each subcircuit represents a portion of the insulated electrode length and has finite width and length. The first subcircuit has the shortest length while the  $N^{\text{th}}$  subcircuit has the longest. Each subcircuit has two capacitors: one for the air above the dielectric and one for the dielectric layer. The plasma resistance is modeled with different values for the forward (positive plasma current) and backward (negative plasma current) portions of the AC cycle. Diodes turn the resistance subcircuits on in the presence of plasma and off in its absence.

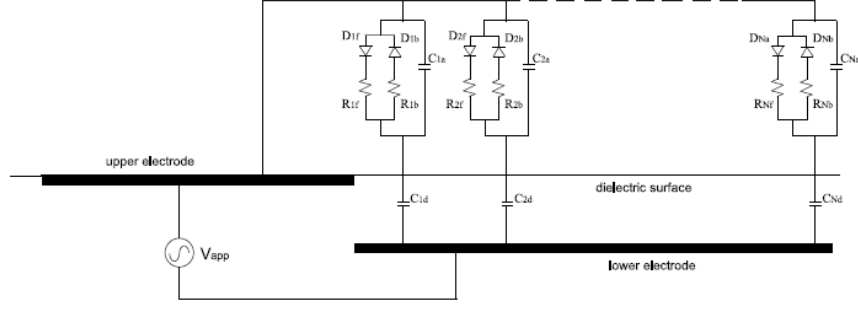


**Figure 3: Parallel Plasma Actuator Circuit Model<sup>8</sup>**

The air capacitance is defined as:

$$C_{an} = \frac{\epsilon_0 \epsilon_a A_n}{l_n} \quad (41)$$

where  $\epsilon_0$  is the permittivity of free space ( $8.854 \times 10^{-12}$  F/m),  $\epsilon_a$  is the dielectric coefficient of air,  $A_n$  is the cross-sectional area of the air capacitor, and  $l_n$  is distance from the edge of the exposed electrode to solution point  $n$  on the dielectric surface.

The dielectric capacitance is:

$$C_{dn} = \frac{\epsilon_0 \epsilon_d A_d}{l_d} \quad (42)$$

Here,  $\epsilon_d$  is the dielectric coefficient of the dielectric material,  $A_d$  is the cross-sectional area of the dielectric capacitor, and  $l_d$  is the thickness of the dielectric material.

The subcircuit resistance is:

$$R_n = \frac{\rho_a l_n}{A_n} \quad (43)$$

where  $\rho_a$  is the resistivity of the air and  $A_n$  and  $l_n$  are the cross-sectional area and length of the subcircuit. Different values are assigned to  $R_n$  depending on the direction of current flow;  $R_{nf}$  is used to denote the resistance for forward plasma current flow, while  $R_{nb}$  is used for backward current flow.

Given a time-dependent applied voltage, the voltage on the dielectric surface in subcircuit  $n$  is described by

$$\frac{dV_n(t)}{dt} = \frac{dV_{app}(t)}{dt} \left( \frac{C_{an}}{C_{an} + C_{dn}} \right) + k_n \left( \frac{I_p(t)}{C_{an} + C_{dn}} \right) \quad (44)$$

where  $k_n = 1$  if plasma is ignited in the circuit and zero otherwise, and the plasma current is given by

$$I_p(t) = \frac{1}{R_n} [V_{app}(t) - V_n(t)] \quad (45)$$

The resistance takes on values  $R_{nf}$  or  $R_{nb}$  depending on the direction of the current in the plasma.

Equation (44) is solved using multistage Runge-Kutta time integration. Then, the applied voltage and the subcircuit voltages are used as boundary conditions in a two-dimensional solution to the Poisson equation, which describes the electric potential  $\phi$ :

$$\frac{\partial^2 \phi}{\partial x^2} + \frac{\partial^2 \phi}{\partial y^2} = \frac{\phi}{\lambda_D^2} \quad (46)$$

The term  $\lambda_D$  is the characteristic length for electrostatic shielding in plasma, called the Debye length.

The solution domain for Eq (46) is a section extracted from the overall Navier-Stokes grid in the immediate vicinity of the plasma actuator. This grid section is subdivided using a nonlinear LaGrange interpolation procedure<sup>12</sup>. Once the body forces have been determined, they are mapped back to the Navier-Stokes grid. This procedure allows the plasma actuator to be modeled in fine detail without requiring the flow solver to operate on an inordinate number of field points. The boundary conditions are applied to the domain boundaries as shown in Figure 4.

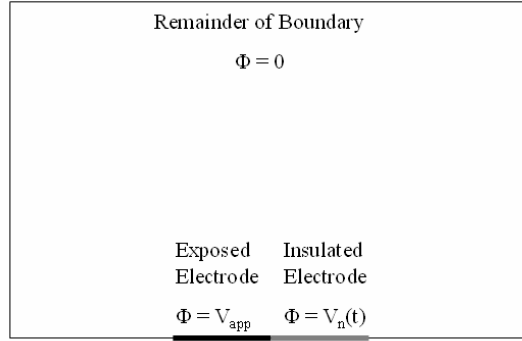


**Figure 4: Poisson Equation Solution Domain with Boundary Conditions**

In practice, the Poisson equation is applied only to the region above the insulated electrode where plasma is present. Elsewhere, the LaPlace equation is solved:

$$\frac{\partial^2 \phi}{\partial x^2} + \frac{\partial^2 \phi}{\partial y^2} = 0 \quad (47)$$

Once Eqs (46) and (47) are solved, the body force *per volume of plasma* at each point in the solution domain can be computed. The electric field  $\vec{E}$  is calculated from the electric potential:

$$\vec{E} = -\vec{\nabla}\phi \quad (48)$$

And the body force is:

$$\vec{f}_b = -\left(\frac{\epsilon_0}{\lambda_D^2}\right)\phi\vec{E} = \left(\frac{\epsilon_0}{\lambda_D^2}\right)\phi\vec{\nabla}\phi \quad (49)$$

Since the computational grids used for real configurations such as airfoils are not Cartesian with even spacing in both coordinate directions, the Poisson/Laplace equations are recast from Cartesian coordinates (x,y)

to general curvilinear coordinates  $(\xi, \eta)$  in the flow solver. The curvilinear coordinate system is Cartesian with uniform spacing of one unit between points in both  $\xi$  and  $\eta$ .

The transformed Poisson equation is<sup>13</sup>

$$J^2(a\phi_{\xi\xi} - 2b\phi_{\xi\eta} + c\phi_{\eta\eta} + d\phi_{\eta} + e\phi_{\xi}) = \frac{\phi}{\lambda_D^2} \quad (50)$$

where

$$J = \frac{1}{x_{\xi}y_{\eta} - y_{\xi}x_{\eta}} \quad (51)$$

$$\begin{aligned} a &= x_{\eta}^2 + y_{\eta}^2 \\ b &= x_{\xi}x_{\eta} + y_{\xi}y_{\eta} \\ c &= x_{\xi}^2 + y_{\xi}^2 \\ d &= J(\alpha y_{\xi} - \beta x_{\xi}) \\ e &= J(\beta x_{\eta} - \alpha y_{\eta}) \end{aligned} \quad (52)$$

and

$$\alpha = ax_{\xi\xi} - 2bx_{\xi\eta} + cx_{\eta\eta} \quad (53)$$

$$\beta = ay_{\xi\xi} - 2by_{\xi\eta} + cy_{\eta\eta} \quad (54)$$

effect the coordinate transformation.

Eq (50) is solved using a finite difference, successive line over-relaxation (SLOR) algorithm. Using the standard finite difference formulae<sup>9</sup>

$$\begin{aligned} \frac{\partial u}{\partial x} &\approx \frac{u_{i+1} - u_{i-1}}{2\Delta x} + O[(\Delta x)^2] \\ \frac{\partial^2 u}{\partial x^2} &\approx \frac{u_{i+1} - 2u_i + 2u_{i-1}}{(\Delta x)^2} + O[(\Delta x)^2] \\ \frac{\partial^2 u}{\partial x \partial y} &\approx \frac{u_{i+1,j+1} - u_{i-1,j+1} - u_{i+1,j-1} + u_{i-1,j-1}}{4\Delta x \Delta y} + O[(\Delta x)^2, (\Delta y)^2] \end{aligned} \quad (55)$$

the discrete form of Eq (50) for solution at the  $i^{\text{th}}$  grid line is

$$-\left(c_{ij} - \frac{d_{ij}}{2}\right)\phi_{i,j-1} + \left[\frac{1}{J^2\lambda_D^2} + 2(a_{ij} + c_{ij})\right]\phi_{ij} - \left(c_{ij} + \frac{d_{ij}}{2}\right)\phi_{i,j+1} = R_{ij} \quad (56)$$

where

$$R_{ij} = a_{ij}(\phi_{i+1,j} + \phi_{i-1,j}) + \frac{e_{ij}}{2}(\phi_{i+1,j} - \phi_{i-1,j}) - \frac{b_{ij}}{2}(\phi_{i+1,j+1} - \phi_{i-1,j+1} - \phi_{i+1,j-1} + \phi_{i-1,j-1}) \quad (57)$$

using the currently available values of  $\phi$ . Eq (57) is solved using the Thomas algorithm for tridiagonal matrices<sup>6</sup>.

The electric field components [Eq (48)] are computed using the following reverse coordinate transformations:

$$\begin{aligned} E_x &= -\phi_x = -(\xi_x \phi_\xi + \eta_x \phi_\eta) \\ E_y &= -\phi_y = -(\xi_y \phi_\xi + \eta_y \phi_\eta) \end{aligned} \quad (58)$$

where

$$\begin{aligned} \xi_x &= Jy_\eta & \xi_y &= -Jx_\eta \\ \eta_x &= -Jy_\xi & \eta_y &= Jx_\xi \end{aligned} \quad (59)$$

In the plasma actuator model supplied by the University of Notre Dame, the sign of the body force is the opposite of that shown in Eq (49). The reason for the body force sign reversal in the Notre Dame code is unknown; this issue had not been resolved with the Notre Dame researchers at the time of this writing.

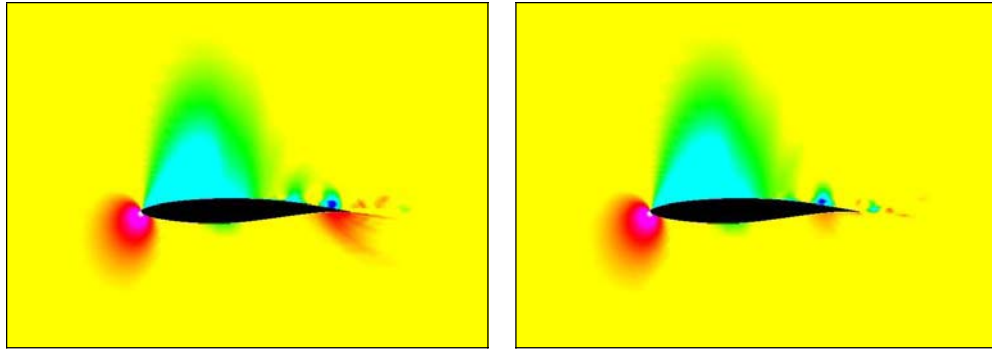
## RESULTS

Two example calculations are presented here. The first is an airfoil flowfield solution, calculated without the plasma actuator model, which demonstrates the accuracy of the flow solver and illustrates the importance of modeling turbulence in the flow solutions. The second solution employs a plasma actuator to induce motion in quiescent air over a flat plate.

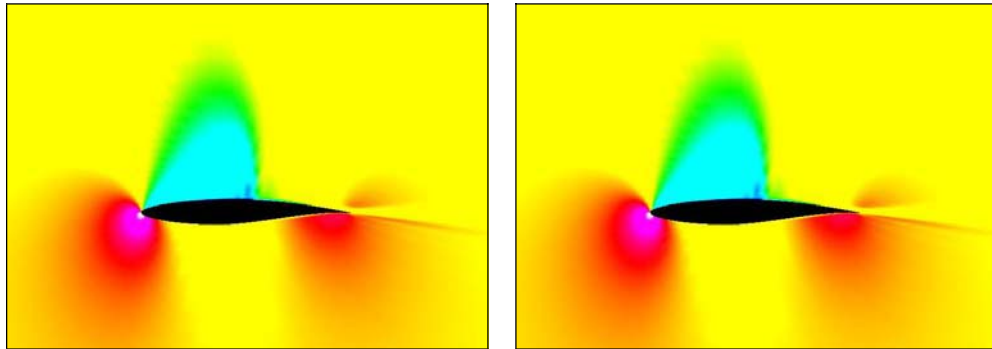
### RAE 2822 Airfoil

Laminar and turbulent solutions for a standard RAE 2822 airfoil CFD code validation case (Mach 0.729,  $\alpha = 2.31^\circ$ ) are contrasted in Figure 5. The surface pressure distributions from the laminar and turbulent solutions are compared to wind tunnel test data for this case in Figure 6. Agreement of the turbulent solution pressure with the data is excellent.

These results illustrate the importance of turbulence modeling for accurate flow characterization. Plasma actuators are being investigated for use in fluid separation control. It is imperative that tools developed to simulate plasma actuator effects adequately model the basic fluid flowfield so that valid conclusions can be drawn from the simulations about the fluid flow manipulation capability of these devices. Separation should only be indicated in the flow simulations in those cases in which separation is likely to occur. In the present case, the laminar solution inaccurately produced large scale flow separation and grossly inaccurate pressure fields. Including turbulence modeling in the simulation eliminated the separation and greatly improved the agreement between the simulation and test data.



(a) Laminar



(b) Turbulent

Figure 5: Laminar and Turbulent Solutions at Corresponding Solution Times for the RAE 2822 Airfoil, Mach 0.729,  $\alpha = 2.31^\circ$

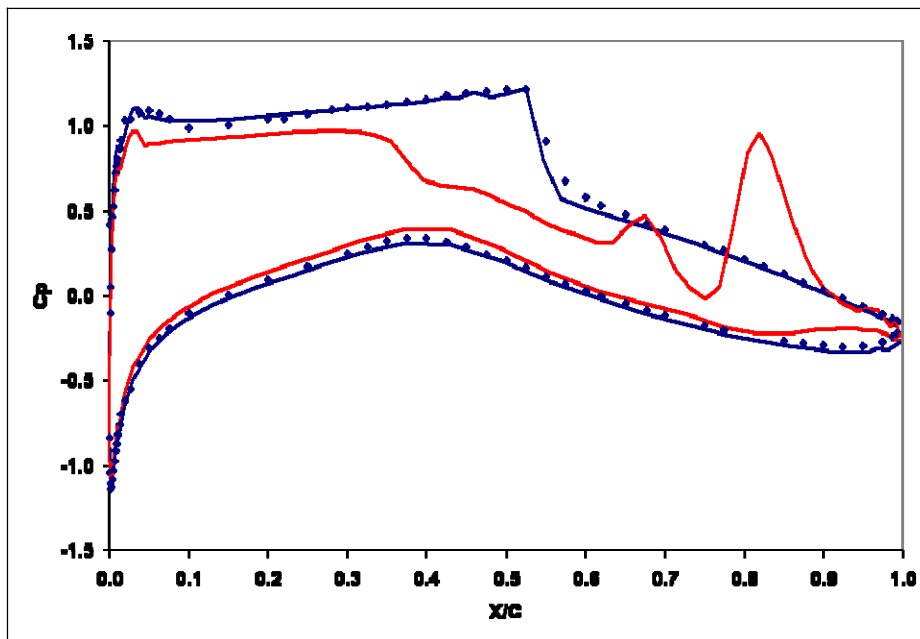
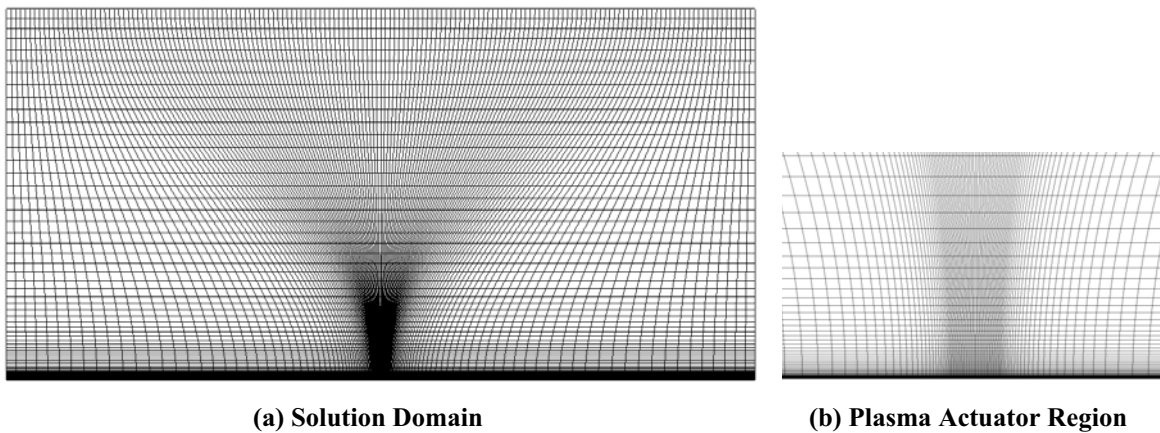


Figure 6: RAE 2822 Airfoil Pressure Data (Points), Laminar Simulation (Red Line) and Turbulent Simulation (Blue Line)

### Flat Plate with Plasma Actuator

The plasma actuator model was tested by evaluating the effect of a plasma actuator mounted on a flat plate on the surrounding quiescent air. The solution domain for this case was very similar to the domain illustrated in Figure 4. Both the exposed and hidden electrodes had a length of  $\frac{1}{2}$  inch (0.0127 m). The dielectric material was 3-mil thick ( $7.62 \times 10^{-5}$  m) Kapton film with a dielectric coefficient of 3.5. The voltage of 5 kV was applied at an AC frequency of 2 kHz.

The  $2\text{m} \times 1\text{m}$ ,  $161 \times 81$  point computational grid was clustered near the plasma actuator, which was centered on the lower boundary of the solution domain. There were 21 evenly spaced points on each electrode. The spacing normal to the wall was a very coarse  $10^{-4}$  m. The computational grid is shown in Figure 7.



**Figure 7: Computational Grid for Plasma Actuator on a Flat Plate**

The flat plate solution was run using a computational time step of  $2 \mu\text{s}$  for 4,000 time steps. The development of a left-to-right near-wall flow is shown in Figure 8 for the first two AC cycles. Note the development and convection of the large initial starting vortex, and the smaller secondary vortex that forms during the second AC cycle. The extent of induced fluid motion at different simulation times is shown in Figure 9. The simulated fluid motion is consistent with the experimental observations of Enloe et al<sup>3</sup>.

### CONCLUSION AND RECOMMENDATIONS

A time-accurate Navier-Stokes flow solver with an integrated plasma actuator body force model has been developed. The base flow solver's accuracy has been demonstrated using standard validation cases. Operation of the plasma actuator model has also been successfully demonstrated, although a thorough validation study has not been conducted.

Since AFOSR is no longer providing funding to AFRL/MNAC for this research, AFRL/MNAC's research effort is being discontinued. However, under an agreement reached with the University of Notre Dame, the code will be provided to researchers there in the hope that it can be fully developed into a useful analysis tool. The following suggestions are offered for future development of the code:

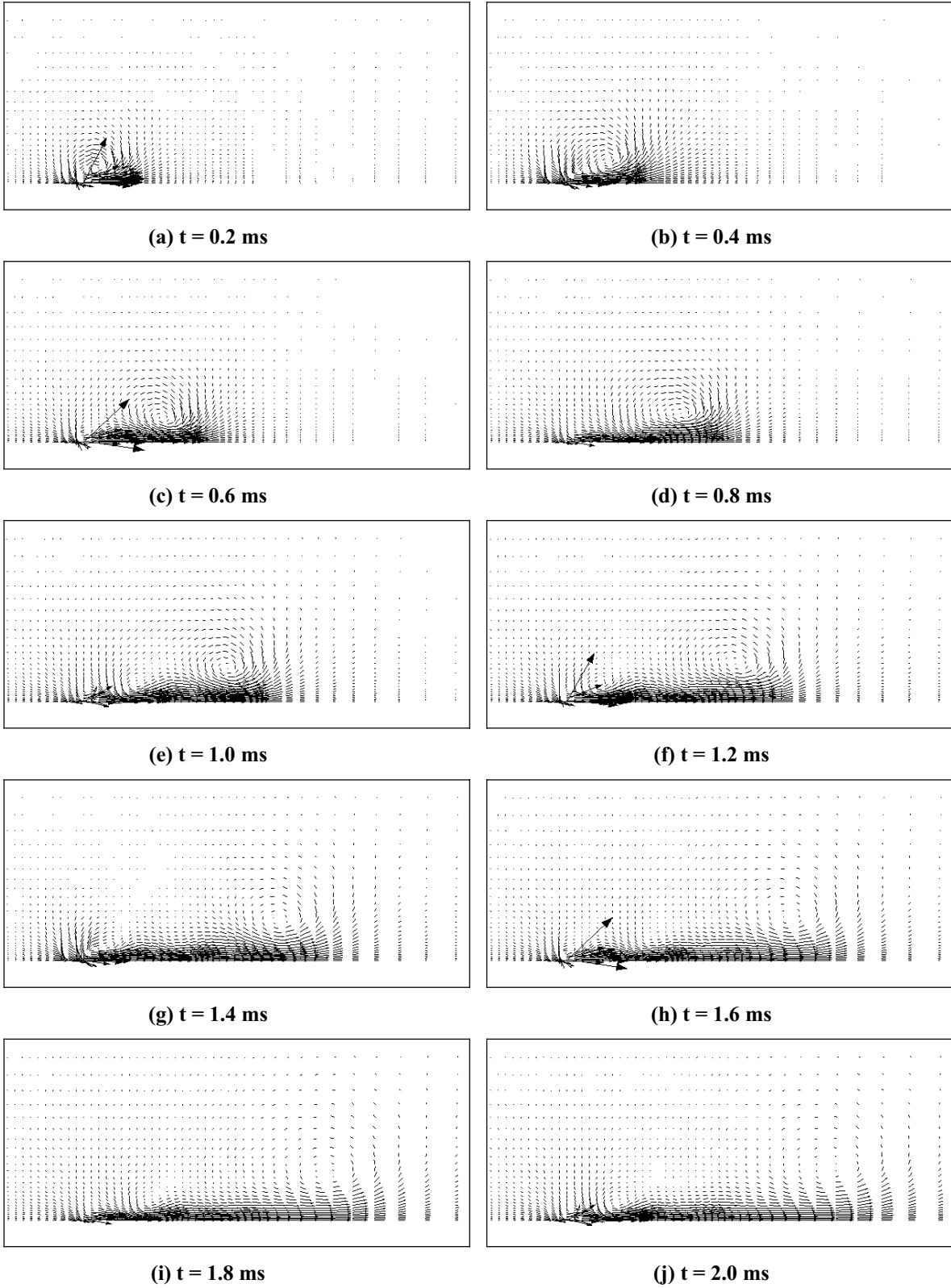
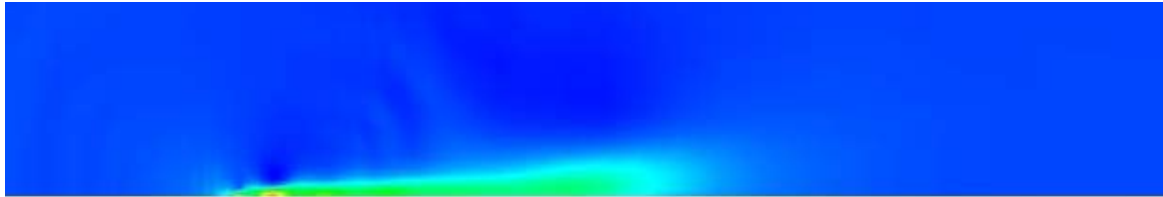


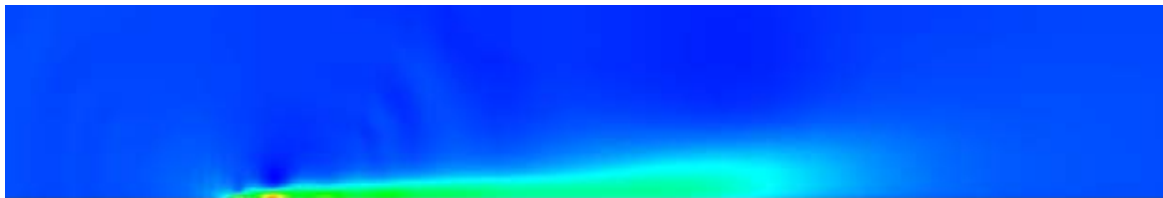
**Figure 8: Near-Wall Momentum Vectors During the First Two Plasma Actuator AC Cycles**



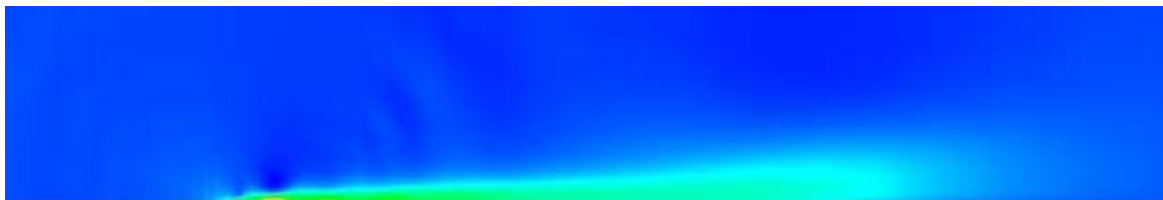
(a)  $t = 2$  ms



(b)  $t = 4$  ms



(c)  $t = 6$  ms



(d)  $t = 8$  ms

**Figure 9: X-Momentum Propagation During the Plasma Actuator Simulation**

- ❖ ***Thorough Validation of the Plasma Actuator Model:*** Although great care was taken in the plasma actuator model implementation, the model originators should carefully examine the code and output to ensure the proper implementation and operation of the plasma actuator model.
- ❖ ***Multiple Boundary Conditions on Grid Boundaries:*** The flow solver currently allows the use of only one boundary condition per grid boundary. This limits the allowable computational grid types to H- and O-topologies. This simple change would allow the use of C-topology grids, which are better suited for airfoil analysis than the presently allowed O-topology grids. This capability was included in a three-dimensional flow solver developed for this research effort and should serve as an example for implementation of a similar capability in the two-dimensional code.
- ❖ ***Characteristic Outer Boundary Condition:*** Currently, only extrapolation and freestream conditions can be imposed at the outer boundary. This introduces a requirement that the outer grid boundary of an airfoil grid must be a great physical distance from the inner grid boundary in order to adequately simulate real

flowfields. This capability was also included in the previously mentioned three-dimensional flow solver and can be easily implemented in the two-dimensional code.

- ❖ ***Multiple Plasma Actuators***: Due to time constraints, this capability was not written into the code. However, such a capability is essential if this analysis capability is to be maximized.
- ❖ ***Parallel Processing Capability***: While the code runs rapidly on a single CPU, analyses could be conducted much more rapidly if this capability was added.

## REFERENCES

1. Hilbun, W. and Case, B., "Preliminary Development of a Computational Model of a Dielectric Barrier Discharge", AIAA Paper 2005-1176, January 2005.
2. Orlov, D., and Corke, T., "Numerical Simulation of Aerodynamic Plasma Actuator Effects", AIAA Paper 2005-1083, January 2005.
3. Enloe, C., McLaughlin, T., VanDyken, R., Kachmer, K., Jumper, E., and Corke, T., "Mechanisms and Responses of a Single Dielectric Barrier Plasma", AIAA Paper 2003-1021, January 2003.
4. Jameson, A., Schmidt, W., and Turkel, E., "Numerical Solution of the Euler Equations by Finite Volume Methods Using Runge-Kutta Time Stepping Schemes", AIAA Paper 81-1259, June 1981.
5. Yoon, S. and Kwak, D., "Artificial Dissipation Models for Hypersonic External Flow", AIAA Paper 88-3708, July 1988.
6. Forsythe, J., Squires, K., Wurtzler, K., and Spalart, P., "Detached-Eddy Simulation of Fighter Aircraft at High Alpha", AIAA Paper 2002-0591, January 2002.
7. Blazek, J., *Computational Fluid Dynamics: Principles and Applications*, Elsevier, 2001.
8. Corke, T. and Orlov, D., "Space-Time Modeling of Dielectric Barrier Discharge Plasma Actuators", Provided via Private Communication.
9. Tannehill, J., Anderson, D., and Pletcher, R., *Computational Fluid Mechanics and Heat Transfer, 2<sup>nd</sup> Ed.*, Taylor and Francis, 1997.
10. Hirsch, C., *Numerical Computation of Internal and External Flows, Volume 1: Fundamentals of Numerical Discretization*, John Wiley and Sons, 1988.
11. Frink, N., Parikh, P. and Pirzadeh, S., "A Fast Upwind Solver for the Euler Equations on Three-Dimensional Unstructured Meshes", AIAA Paper AIAA-91-0102, January 1991.
12. Botha, J. and Pinder, G., *Fundamental Concepts in the Numerical Solution of Differential Equations*, John Wiley and Sons, 1983.
13. Hoffman, K. and Chiang, S., *Computational Fluid Dynamics, Volume I, 4<sup>th</sup> Ed.*, Engineering Education System, 2000.

## **ACKNOWLEDGEMENTS**

The two-dimensional flow solver described herein was funded by the Air Force Office of Scientific Research. The plasma actuator model was provided by Dr. Thomas Corke and Mr. Dmitriy Orlov of the University of Notre Dame.



